Spin-resolved nonequilibrium thermopower of asymmetric nanojunctions

Anand Manaparambil* and Ireneusz Weymann
Institute of Spintronics and Quantum Information, Faculty of Physics, Adam Mickiewicz University, Uniwersytetu Poznańskiego 2, 61-614 Poznań, Poland

(Received 31 July 2023; revised 20 January 2024; accepted 16 February 2024; published 4 March 2024)

The spin-resolved thermoelectric transport properties of correlated nanoscale junctions, consisting of a quantum dot/molecule asymmetrically coupled to external ferromagnetic contacts, are studied theoretically in the far-from-equilibrium regime. One of the leads is assumed to be strongly coupled to the quantum dot resulting in the development of the Kondo effect. The spin-dependent current flowing through the system, as well as the thermoelectric properties, are calculated by performing a perturbation expansion with respect to the weakly coupled electrode, while the Kondo correlations are captured accurately by using the numerical renormalization group method. In particular, we determine the differential and nonequilibrium Seebeck effects of the considered system in different magnetic configurations and uncover the crucial role of spin-dependent tunneling on the device performance. Moreover, by allowing for the spin accumulation in the leads, which gives rise to finite spin bias, we shed light on the behavior of the nonequilibrium spin Seebeck effect. In particular, we predict new sign changes of the spin-resolved Seebeck effect in the nonlinear response regime, which stem from the interplay of exchange field and finite voltage and temperature gradients.

DOI: 10.1103/PhysRevB.109.115402

I. INTRODUCTION

Quantum transport through nanojunctions containing quantum dots or molecules has been under tremendous research interest due to promising applications of such nanostructures in nanoelectronics, spintronics, and spin caloritronics [1–4]. Due to the strong electron-electron interactions and a characteristic discrete density of states, these systems can exhibit large thermoelectric figure-of-merit and are excellent candidates for nanoscale heat engines [5–10]. As far as more fundamental aspects are concerned, correlated nanoscale systems enable exploration of fascinating many-body phenomena in a controllable fashion, which is hardly possible in bulk materials. One such phenomena is the Kondo effect [11,12], which can drastically change the system's transport properties at low temperatures by giving rise to a universal enhancement of the conductance to its maximum [13,14]. In addition to voltage-biased setups' investigations, the emergence of Kondo correlations can be also probed in the presence of a temperature gradient, where thermoelectric transport properties reveal the important physics [6–8]. In fact, the thermopower of quantum dot and molecular systems has been shown to contain the signatures of the Kondo phenomenon. More specifically, the sign changes in the temperature dependence of the Seebeck coefficient with the onset of Kondo correlations have been identified in both theoretical [15] and experimental [16–18] studies.

Further interesting properties arise when the junction's electrodes are ferromagnetic and the tunneling processes become spin-dependent [1,3,4,19]. In the presence of a finite temperature gradient, one can then observe an intricate interplay of heat, charge, and spin, which gives rise to the emergence of the spin Seebeck effect [20,21]. Besides this fundamental phenomenon, which is of interest for spin caloritronics [2], ferromagnetic nanojunctions allow for the exploration of competition between the Kondo correlations and the so-called ferromagnet-induced exchange field, which acts as a local magnetic field that can suppress the Kondo effect [22–25]. Such competition has already been revealed in theoretical studies on thermoelectric properties of various strongly correlated molecular and quantum dot systems with ferromagnetic contacts [26–34]. Most of these investigations, however, concerned the case of the linear response regime. As far as fully out-of-equilibrium settings are concerned, there have already been some efforts to understand nonlinear thermopower of nonmagnetic junctions [35–40], while the spin-dependent thermoelectric properties of ferromagnetic nanojunctions remain to a large extent unexplored.

The primary goal of this work is therefore to analyze the spin-resolved nonequilibrium thermopower of correlated nanoscale junctions, in which the interplay between the Kondo and exchange field is relevant. In particular, we study thermoelectric characteristics of nanojunctions that exhibit asymmetry in the couplings to ferromagnetic metallic leads. Such asymmetric couplings can be encountered especially in molecular junctions [41–46], and can be also present in artificial heterostructures with quantum dots by appropriately adjusting the gate voltages [47–49]. We thus consider a quantum dot/molecule strongly coupled to one ferromagnetic lead and weakly coupled to the other nonmagnetic or ferromagnetic lead kept at different potentials and temperatures, as displayed in Fig. 1. To determine the current flowing through such system, we perform a perturbation

*anaman@amu.edu.pl

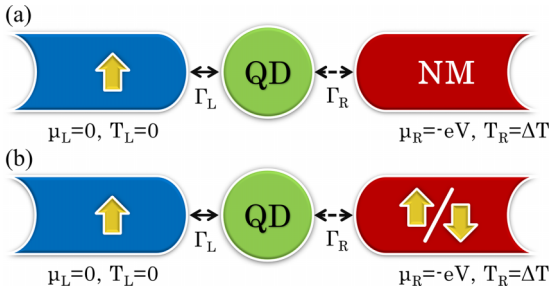

FIG. 1. The schematic of the considered asymmetric tunnel junction with embedded quantum dot/molecule strongly coupled to a cold ferromagnetic left lead and weakly coupled to a hot (a) nonmagnetic or (b) ferromagnetic right lead. The right lead is subject to voltage and temperature gradients, while the left lead is grounded and kept at zero temperature. The device in (b) can be in two magnetic configurations: the parallel (P) and antiparallel (AP) one, as indicated by the arrows.

expansion with respect to the weak coupling, while the properties of the strongly coupled subsystem, in which the Kondo correlations may arise, are obtained with the aid of the numerical renormalization group (NRG) method [50,51]. This allows us to accurately explore the signatures of the interplay between the spin-resolved transport and the Kondo correlations in the Seebeck coefficient. Furthermore, we study how different magnetic configurations of the system affect the differential and nonequilibrium Seebeck effects of the system. In particular, we show that the Seebeck coefficient exhibits new sign changes as a function of the bias voltage, which can be associated with the Kondo resonance split by exchange field. These sign changes are found to extend to the temperature gradients on the order of the Kondo temperature. Moreover, we provide a detailed analysis of the nonequilibrium spin Seebeck coefficient and demonstrate that it exhibits new sign changes in the nonlinear response regime, which stem from the interplay of spin-resolved tunneling and finite voltage and temperature gradients.

The paper is organized as follows: The system Hamiltonian and the theoretical framework are described in Sec. II. The numerical results and their discussion are presented in Sec. III, where we first analyze the exchange field effects on nonequilibrium thermopower, then, we consider the role of different magnetic configurations and, finally, we present the behavior of the nonlinear spin Seebeck effect. The summary and concluding remarks can be found in Sec. IV.

II. THEORETICAL DESCRIPTION

A. Model and Hamiltonian of the system

We consider a nanoscale junction with an embedded quantum dot/molecule, which is schematically shown in Fig. 1. The quantum dot is assumed to be strongly coupled to the left ferromagnetic lead and weakly coupled to the right lead, which can be either nonmagnetic [Fig. 1(a)] or ferromagnetic [Fig. 1(b)]. In the case of two ferromagnetic electrodes, we will distinguish two magnetic configurations: the parallel (P) one when the leads magnetic moments point in the same direction and the antiparallel (AP) one, when the orientation of magnetic moments is opposite, see Fig. 1(b). It is assumed that there are finite temperature and voltage gradients applied to the system, with $T_L = 0$ and $\mu_L = 0$, whereas $T_R = \Delta T$ and $\mu_R = -eV$, as shown in Fig. 1, where T_α and μ_α are the temperature ($k_B \equiv 1$) and the chemical potential of lead α.

With the assumption of weak coupling between the quantum dot and right contact the system Hamiltonian can be simply written as

$$H = H_L + H_R + H_T. \tag{1}$$

H_L describes the strongly coupled left subsystem, consisting of the quantum dot and the left lead, and it is given by

$$H_L = \varepsilon_d \sum_\sigma n_\sigma + U n_\uparrow n_\downarrow + \sum_{k\sigma} \varepsilon_{Lk\sigma} c^\dagger_{Lk\sigma} c_{Lk\sigma} + \sum_{k\sigma} t_{Lk\sigma} (d^\dagger_\sigma c_{Lk\sigma} + c^\dagger_{Lk\sigma} d_\sigma), \tag{2}$$

where $n_\sigma = d^\dagger_\sigma d_\sigma$, with $d^\dagger_\sigma$ (d_σ) being the creation (annihilation) operator on the quantum dot for an electron of spin σ, $c_{\alpha k\sigma}$ ($c^\dagger_{\alpha k\sigma}$) annihilates (creates) an electron in the lead α with momentum k, spin σ and energy $\varepsilon_{\alpha k\sigma}$. The quantum dot is modeled by a single orbital of energy ε_d and Coulomb correlations U. The hopping matrix elements between the quantum dot and lead α are denoted by $t_{\alpha k\sigma}$ and give rise to the level broadening $\Gamma_{\alpha\sigma} = \pi \rho_{\alpha\sigma} |t_{\alpha k\sigma}|^2$, which is assumed to be momentum independent, where $\rho_{\alpha\sigma}$ is the density of states of lead α for spin σ.

The second part of the Hamiltonian describes the right lead and is given by

$$H_R = \sum_{k\sigma} (\varepsilon_{Rk\sigma} - \mu_R) c^\dagger_{Rk\sigma} c_{Rk\sigma}, \tag{3}$$

while the last term of H accounts for the hopping between the left and right subsystems

$$H_T = \sum_{k\sigma} t_{Rk\sigma} (d^\dagger_\sigma c_{Rk\sigma} + c^\dagger_{Rk\sigma} d_\sigma). \tag{4}$$

In the following, we use the lowest-order perturbation theory in H_T to study the spin-dependent electric and thermoelectric properties of the system.

B. Method and nonlinear transport coefficients

The electric current flowing through the system in the spin channel σ in the lowest-order perturbation with respect to the coupling to the right lead can be expressed as [52,53]

$$I_\sigma(V, \Delta T) = -\frac{e\Gamma_{R\sigma}}{\hbar} \int_{-\infty}^{\infty} d\omega\, A_{L\sigma}(\omega) \times [f_L(\omega) - f_R(\omega - eV)], \tag{5}$$

where $f_\alpha(\omega) = [1 + \exp(\omega/T_\alpha)]^{-1}$ is the Fermi-Dirac distribution function, while $A_{L\sigma}(\omega)$ denotes the spin-resolved spectral function of the left subsystem. The total current flowing through the system under potential bias V and temperature gradient ΔT is thus $I(V, \Delta T) = \sum_\sigma I_\sigma(V, \Delta T)$. Since we treat the coupling to the right lead as a perturbation, we expect the next-order contributions, e.g., $I_\sigma \sim \Gamma^2_{R\sigma}$, to be much smaller, and assume that these do not affect the main behavior of the system.

The spectral function of the left subsystem $A_{L\sigma}(\omega)$ is calculated by means of the NRG method [50,51,54], which allows us to include all the correlation effects between the quantum dot strongly coupled to the left contact in a fully nonperturbative manner. The spectral function $A_{L\sigma}(\omega)$ is determined as the imaginary part of the Fourier transform of the retarded Green's function of the left subsystem Hamiltonian, H_L, $G_\sigma(t) = -i\Theta(t)\langle\{d_\sigma(t), d_\sigma^\dagger(0)\}\rangle$. For the purpose of NRG calculations, the conduction band of the left lead can be discretized logarithmically with discretization parameter Λ and mapped onto a tight binding chain (Wilson chain) with couplings that decay as $\Lambda^{-n/2}$, where n is the site number in the chain. This mapping transforms H_L into a tight-binding Hamiltonian with each quantum dot spin σ coupled to the first site of the chain with an effective coupling $\sqrt{2\Gamma_{L\sigma}/\pi}$. The new Hamiltonian is then solved iteratively, while keeping a relevant number of the lowest energy eigenstates N_K. In our calculations, we use $\Lambda = 2$, the iteration number $N = 60$ and the kept states N_K at least 2^{10}. To obtain the spectral function, the data is collected in logarithmic bins that are then appropriately broadened to obtain a smooth function [55]. We note that in general the spectral function also depends on temperature, however, to shed light on the Kondo correlations in thermoelectric transport behavior, we assume that the left lead temperature is well below the Kondo temperature, T_K. Hence, the spectral function for $T_L \ll T_K$ is essentially equivalent to the zero-temperature spectral function.

For the further analysis, it is convenient to express the coupling constants $\Gamma_{\alpha\sigma}$ by using the spin polarization of the lead α, p_α, as $\Gamma_{L\sigma} = (1 + \sigma p_L)\Gamma_L$ and $\Gamma_{R\sigma} = (1 + \sigma p_R)\Gamma_R$ for the parallel magnetic configuration, with $\Gamma_{R\sigma} = (1 - \sigma p_R)\Gamma_R$ in the case of the antiparallel configuration of the system. Here, $\Gamma_\alpha = (\Gamma_{\alpha\uparrow} + \Gamma_{\alpha\downarrow})/2$. Furthermore, in the case when the right lead is nonmagnetic, $p_R = 0$, while for both ferromagnetic leads we for simplicity assume $p_L = p_R \equiv p$.

As far as thermoelectric coefficients are concerned, the differential Seebeck coefficient can be expressed as [56]

$$S_d = -\left(\frac{dV}{d\Delta T}\right)_I = -\left(\frac{\partial I}{\partial \Delta T}\right)_V \Big/ \left(\frac{\partial I}{\partial V}\right)_{\Delta T}. \tag{6}$$

Furthermore, the extension of the conventional Seebeck coefficient to the nonlinear response regime is referred to as the nonequilibrium Seebeck coefficient S_n, and it can be defined as [39,47,49,57–59]

$$S_n = -\left(\frac{\Delta V}{\Delta T}\right)_{I(V+\Delta V,\Delta T)=I(V,0)}. \tag{7}$$

The above definitions will be used to describe thermoelectric transport in different configurations of the system, respectively.

III. NUMERICAL RESULTS AND DISCUSSION

In this section we present the main numerical results and their discussion. In our considerations we assume that the left lead is always ferromagnetic, while the right electrode can be either nonmagnetic or ferromagnetic, cf. Fig. 1. For the studied setup, the strong coupling to the left contact may give rise to the Kondo effect [12,13]. However, it is crucial to realize that the presence of the spin-dependent hybridization results in a local exchange field on the quantum dot, which can split the dot orbital level when detuned from the particle-hole symmetry point, and thus suppress the Kondo resonance. The magnitude of such exchange field can be estimated from the perturbation theory, which at zero temperature gives [60],

$$\Delta\varepsilon_{\rm exch} = \frac{2p_L\Gamma_L}{\pi} \ln\left|\frac{\varepsilon_d}{\varepsilon_d + U}\right|. \tag{8}$$

The presence of the exchange field and its detrimental effect on the Kondo phenomenon has been confirmed by various experiments on electronic transport measurements in quantum dot and molecular systems [23,24,61,62].

We start our considerations with the analysis of electric transport properties, revealing the effects of the exchange field. Further on, we study the nonlinear thermoelectric response, first for the case of nonmagnetic right lead and then for the case of two ferromagnetic leads. In numerical calculations, we use the following parameters: $U = 0.2$, $\Gamma_L = 0.02$, $\Gamma_R = 0.002$, in units of band halfwidth, and $p = 0.4$ for the ferromagnetic leads. For the assumed parameters, the Kondo temperature of the left subsystem for $\varepsilon_d = -U/2$ is equal to [60,63], $T_K \approx 0.035\Gamma_L$. We notice that one could, in principle, expect that the coupling to the right contact should also give rise to the Kondo correlations. However, due to exponential dependence of T_K on the ratio of Coulomb correlations and coupling strength, the estimated right-lead Kondo temperature is completely negligible. Thus, it is fully justifiable to assume that the Kondo correlations result only from the coupling to the left lead.

To begin with, it is instructive to analyze the properties of the left subsystem itself as described by its local density of states. The spectral function for each individual spin channel is shown in Fig. 2. First of all, one can see that for $\varepsilon_d = -U/2$, there is a pronounced Kondo peak at the Fermi level for each spin component. However, when detuned from the particle-hole symmetry, a finite exchange-induced splitting emerges, cf. Eq. (8), which suppresses the Kondo effect when $|\Delta\varepsilon_{\rm exch}| \gtrsim T_K$. Because of that, each spin component of the spectral function displays a slightly detuned from Fermi energy side peak, constituting the split Kondo resonance. In addition, the Hubbard resonances at $\omega \approx \varepsilon_d$ and $\omega \approx \varepsilon_d + U$ become affected as well: although their position is only slightly modified, their magnitude gets strongly spin-dependent.

The splitting of the Kondo resonance is directly visible in the differential conductance of the system, which is displayed in Fig. 3. This figure presents the bias voltage dependence of the differential conductance in different magnetic configurations for various temperature gradients, as indicated. More specifically, G corresponds to the case when the right lead is nonmagnetic [cf. Fig. 1(a)], while G^P (G^{AP}) presents the case of both ferromagnetic leads in the parallel (antiparallel) alignment [cf. Figs. 1(b)–1(c)]. When the orbital level is detuned out of the particle-hole symmetry point, the splitting of the Kondo resonance may emerge depending on the magnetic configuration of the system. The behavior of the differential conductance at low bias voltage is displayed in the insets of Fig. 3.

Let us begin the discussion with the case of nonmagnetic right lead, presented in Fig. 3(a). First of all, one can note a

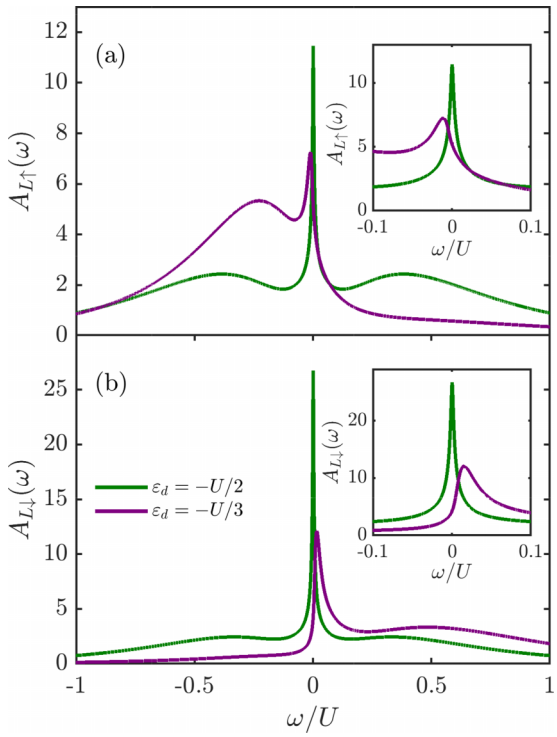

FIG. 2. The energy dependence of the spectral functions for the individual spin channels, (a) $A_{L\uparrow}(\omega)$ and (b) $A_{L\downarrow}(\omega)$ calculated for the strongly coupled left subsystem with orbital energies as indicated. The zoomed Kondo and split-Kondo peaks are shown in the insets. The other parameters are: $U = 0.2$, $\Gamma_L = 0.02$, in units of band half width, and $p = 0.4$.

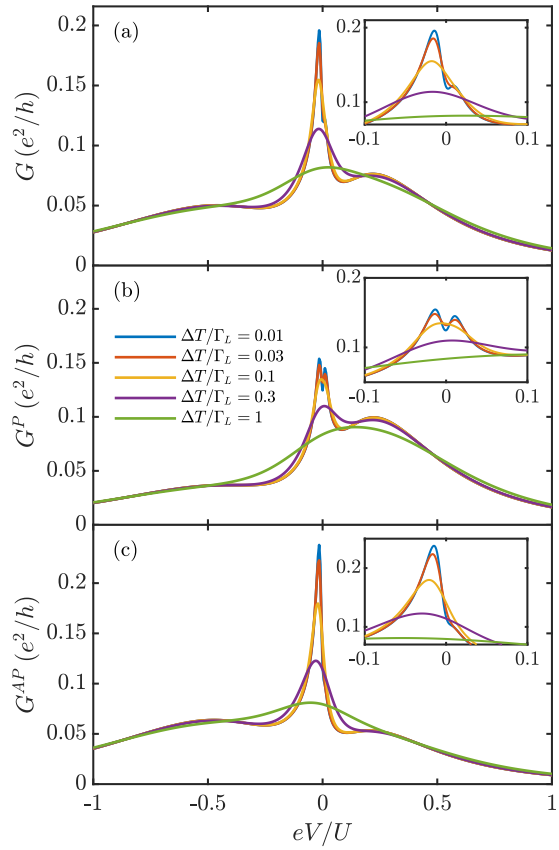

FIG. 3. The differential conductance for the quantum dot strongly coupled to ferromagnetic left lead and weakly coupled to (a) nonmagnetic right lead, ferromagnetic right lead in (b) the parallel, and (c) antiparallel magnetic configuration. The insets show the closeup of the differential conductance behavior for respective configurations. The parameters are the same as in Fig. 2 with $\varepsilon_d = -U/3$, $\Gamma_R = 0.002$, and different temperature gradients, as indicated.

large asymmetry of the differential conductance with respect to the bias reversal. Moreover, for small temperature gradients, $\Delta T \lesssim T_K$, the split zero-bias anomaly due to the Kondo effect is visible. To qualitatively understand this behavior, it is helpful to inspect the behavior of the spectral function around the Fermi energy, see the insets of Fig. 2. One can note that the split Kondo peak in $A_{L\uparrow}(\omega < 0)$ has a smaller weight compared to the split Kondo peak in $A_{L\downarrow}(\omega > 0)$. Because, for low temperature gradients, for $eV > 0$ ($eV < 0$), we probe the density of states of the left subsystem for negative (positive) energies, the above-mentioned asymmetry in $A_{L\sigma}(\omega)$ gives rise to highly asymmetric behavior of the differential conductance, see Fig. 3(a), with the peak in the negative voltage regime more pronounced than the other. Interestingly, when the tunneling to the right lead becomes spin dependent, in the case of parallel configuration one observes a rather symmetric behavior of G^P, with nicely visible split zero-bias anomaly, see Fig. 3(b). This is due to the fact that the increased tunneling rate of spin-down electrons due to larger density of states becomes now reduced since the spin-down electrons are the minority ones in the right lead. On the other hand, the tunneling of spin-up electrons to the right is enlarged. As a consequence, the unequal contributions of the currents in each spin channel become now equalized and the differential conductance in the parallel configuration exhibits split-Kondo resonance with the side peaks of comparable height. On the other hand, when the magnetization of the right lead is flipped, the asymmetric behavior visible in Fig. 3(a) is even further magnified, see Fig. 3(c). This can be understood by invoking similar arguments as above, keeping in mind that now the rate of spin-up tunneling to the right lead is smaller than that for the spin-down electrons. With increase in the temperature gradient, the Kondo-related behavior gets smeared and finally disappears when $\Delta T \gtrsim T_{\rm K}, |\Delta\varepsilon_{\rm exch}|$.

A. Effects of exchange field on nonequilibrium thermopower

In this section, we focus on the case where the right lead is nonmagnetic, see Fig. 1(a). In such a setup it will be possible to observe clear signatures of ferromagnet-induced exchange field on the thermoelectric properties of the system subject to temperature and voltage gradients. We first study the case of the linear response in potential bias with nonlinear temperature gradient in Sec. III A 1, while in Sec. III A 2 the discussion is extended to the case of nonlinear response regime in both ΔT and V.

1. Zero-bias thermoelectrics with finite temperature gradient

Figure 4 displays the zero-bias differential conductance G, the differential Seebeck coefficient $S_{\rm d}$ and the nonlinear

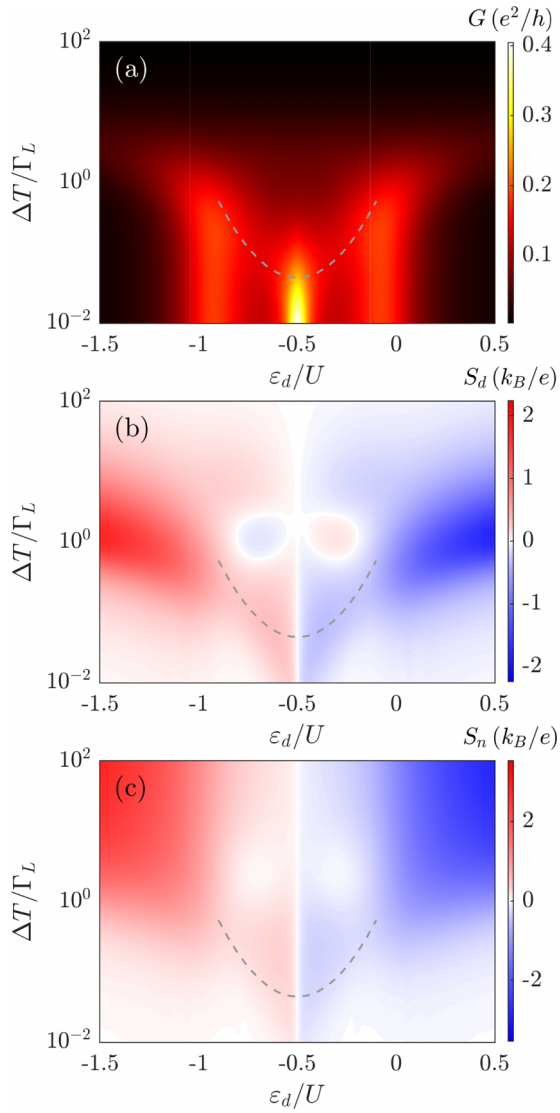

FIG. 4. (a) The differential conductance G, (b) the differential Seebeck coefficient S_d, and (c) the nonequilibrium Seebeck coefficient S_n of the quantum dot strongly coupled to left ferromagnetic lead and weakly attached to the right nonmagnetic lead plotted as a function of the orbital energy ε_d and the temperature gradient ΔT. The dashed lines show the Kondo temperature for the corresponding parameters. The system is assumed to be in the linear response regime with respect to the bias voltage. The other parameters are the same as in Fig. 3.

Seebeck coefficient $S_{\rm n}$ calculated as a function of orbital level ε_d and finite temperature gradient ΔT. For low temperature gradients, the conductance shows considerable increase near three values of ε_d. The peaks for $\varepsilon_d \approx 0$ and $\varepsilon_d \approx -U$ correspond to the Hubbard resonances, whereas the maximum at $\varepsilon_d = -U/2$ is due to the Kondo effect. In fact, in the local moment regime, $-1 \lesssim \varepsilon_d/U \lesssim 0$, the Kondo resonance is suppressed by the exchange field once $|\Delta\varepsilon_{\rm exch}| \gtrsim T_K$, i.e., for values of ε_d away from the particle-hole symmetry point, cf. Eq. (8). With the increase in the temperature gradient, the Kondo resonance dies out when $\Delta T > T_K$, see the dashed line in the figure, and the Hubbard peaks get suppressed when $\Delta T > \Gamma_L$, see Fig. 4(a).

In the case of differential and nonlinear Seebeck coefficients presented in Figs. 4(b) and 4(c), respectively, we can see an overall antisymmetric behavior across the particle-hole symmetry point $\varepsilon_d = -U/2$. The sign of the Seebeck coefficient here corresponds to the dominant charge carriers in transport, holes for $\varepsilon_d < -U/2$ and particles for $\varepsilon_d > -U/2$. The differential Seebeck coefficient shows two sign changes in the local moment regime as a function of the temperature gradient. Typically, in the linear response regime, the sign change at the lower temperature gradient corresponds to the Kondo correlations and is seen around the Kondo temperature T_K [15]. However, in our system the exchange field suppresses and splits the Kondo resonance, such that the signatures of the Kondo correlations are seen at $\Delta T \approx \Gamma_L$, which is much larger than $\Delta T \approx T_K$. In the case of nonlinear Seebeck coefficient, we do not find the corresponding sign changes because $S_{\rm n}$ can deviate considerably from the linear response Seebeck coefficient at large ΔT [33]. Additionally, one can see that both Seebeck coefficients decay with decreasing ΔT. This behavior can be captured using the Sommerfeld expansion for the linear response Seebeck coefficient

$$S(T) \propto \frac{T}{A(\omega = 0, T)} \frac{\partial A}{\partial \omega}\bigg|_{\omega=0}. \tag{9}$$

We also note that both Seebeck coefficients can possess finite values at even lower ΔT inside the local moment regime than outside of it, due to the additional contribution associated with the Kondo effect.

2. *The case of nonlinear potential bias and temperature gradients*

Let us now inspect the behavior of the nonequilibrium thermoelectric coefficients as a function of both potential bias and temperature gradient shown in Fig. 5, focusing on V and ΔT range where Kondo correlations are important. The first row of the figure corresponds to the case of particle-hole symmetry, $\varepsilon_d = -U/2$, while the second row presents the results for $\varepsilon_d = -U/3$. Consider the first case. Figure 5(a) depicts the bias and temperature gradient dependence of the differential conductance G. There exist a prominent peak at low ΔT centered at $V = 0$, this is the zero-bias conductance peak characteristic of the Kondo effect. As the temperature gradient increases, the Kondo peak dies out and becomes smeared when $\Delta T \gtrsim T_K$. It is important to note that the increase in the temperature of the right lead does not suppress the Kondo resonance in the strongly correlated left subsystem. Finite T_R rather obscures the characteristics of the Kondo effect by smearing the transport window defined by $[f_L(\omega) - f_R(\omega - eV)]$, cf. Eq. (5). The differential and nonlinear Seebeck coefficients, shown in Figs. 5(b) and 5(c), exhibit a sign change with respect to the bias voltage reversal. Moreover, while S_d exhibits considerable values around the Kondo peak and becomes suppressed as ΔT grows, S_n gets enhanced when $\Delta T \gtrsim (\Gamma_L/U)|eV|$.

When the orbital level is detuned out of the particle-hole symmetry point, one can observe an interesting interplay between the exchange field and Kondo effect, and its signatures present in the nonlinear thermoelectric coefficients. First,

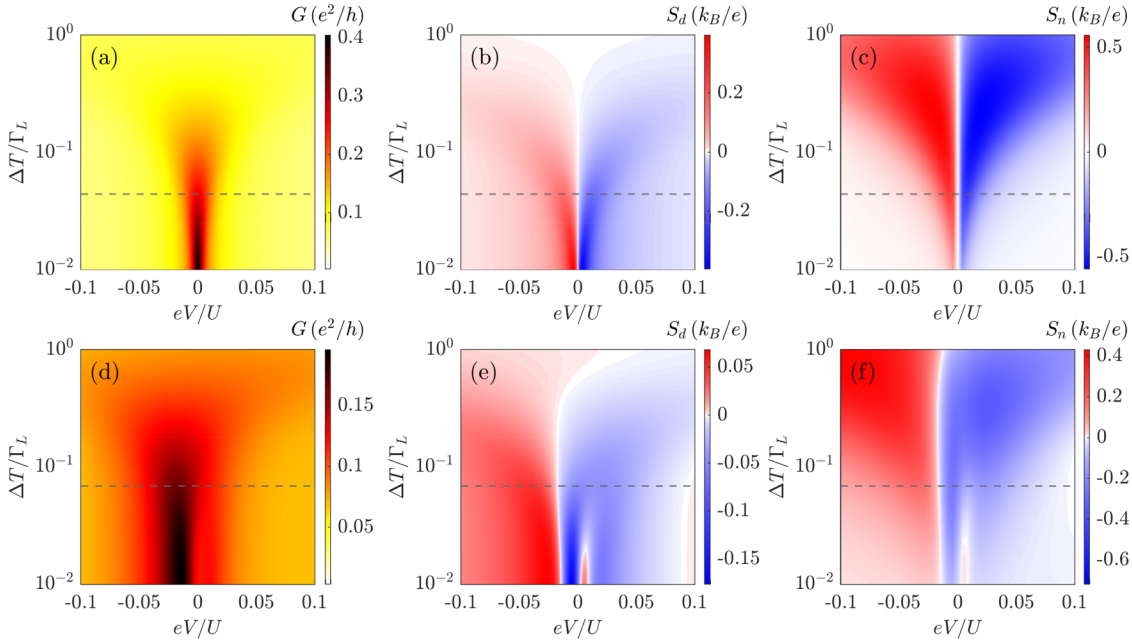

FIG. 5. (a), (d) The differential conductance G, (b), (e) the differential Seebeck coefficient S_d and (c), (f) the nonequilibrium Seebeck coefficient S_n as a function of the potential bias V and the temperature gradient ΔT. The first row corresponds to the particle-hole symmetry point $\varepsilon_d = -U/2$, while the second row shows the case of $\varepsilon_d = -U/3$. The dashed horizontal lines indicate the Kondo temperature T_K for the corresponding ε_d. The other parameters are the same as in Fig. 3.

Fig. 5(d) shows the splitting of the Kondo peak due to the exchange field present in the strongly correlated subsystem. As observed in the discussions of Fig. 3(a), the split Kondo peaks are not symmetric, with the more prominent one in the $eV < 0$ regime and both dying off at large ΔT. Interestingly, the differential and nonlinear Seebeck coefficients also capture the signatures of the exchange field shown by the split Kondo peak. In fact, there exist additional sign changes in the nonlinear response regime with respect to V. More specifically, at low ΔT, there is a sign change at low bias voltages, followed by another one, roughly located around the split-Kondo peak, see Figs. 5(e) and 5(f). These sign changes correspond to the additional energy scale in the system, namely the exchange field $\Delta\varepsilon_{\rm exch}$. They occur at slightly different absolute values of eV, which is due to the fact that the Kondo resonance exhibits an asymmetric splitting, cf. Fig. 2. With increasing the temperature gradient, we observe that the right split Kondo peak in the conductance dies out first, accordingly the regime of positive values of the Seebeck coefficients corresponding to the right peak disappears around $\Delta T \approx 0.03\Gamma_L$. Moreover, we also note that the overall sign change of the thermopower as a function of the bias voltage is now shifted to negative values of eV, as compared to the case of particle-hole symmetry, see Fig. 5.

B. Effects of different magnetic configurations on nonequilibrium thermopower

In this section we study the case where the quantum dot is coupled to both ferromagnetic leads with spin polarization $p = 0.4$. The magnetic moments of the external leads are assumed to be aligned either in parallel or antiparallel. The focus is on the effects of different magnetic configurations on nonequilibrium thermoelectric transport properties.

1. The case of zero bias with nonlinear temperature gradient

The zero-bias thermoelectric properties of the system with two ferromagnetic leads are shown in Fig. 6. The differential conductance for the parallel G^P and antiparallel G^{AP} configuration of the lead magnetizations is shown in Figs. 6(a) and 6(b). The qualitative behavior of both conductances is similar to the case of nonmagnetic lead on the right, where G shows a region of high conductance around $\varepsilon_d = -U/2$ due to the Kondo effect. Similarly to the previous case, the exchange field suppresses the linear response conductance for values of ε_d away from the particle-point symmetry point. Around $\varepsilon_d \approx 0, -U$, there is am increase in the conductance corresponding to the contribution from the Hubbard peaks. It is interesting to note that the conductance in the case of parallel configuration is smaller than that in the antiparallel configuration around the Kondo resonance, cf. the discussion of Fig. 3, while this situation is reversed for the resonances at $\varepsilon_d \approx 0, -U$.

The Seebeck coefficients S_d^P and S_n^P shown in Figs. 6(c) and 6(e) for the parallel configuration display very interesting features corresponding to various energy scales. These coefficients show antisymmetric behavior across $\varepsilon_d = -U/2$ and sign changes as a function of temperature gradient in the local moment regime $-1 \lesssim \varepsilon_d/U \lesssim 0$. Let us first consider the linear response in ΔT for S_d^P. In this regime one can relate the Seebeck coefficient to the conductance through the Mott's formula. Thus, the changes of G^P as a function of orbital level are reflected in the corresponding dependence of the thermopower, which shows sign changes as ε_d is detuned

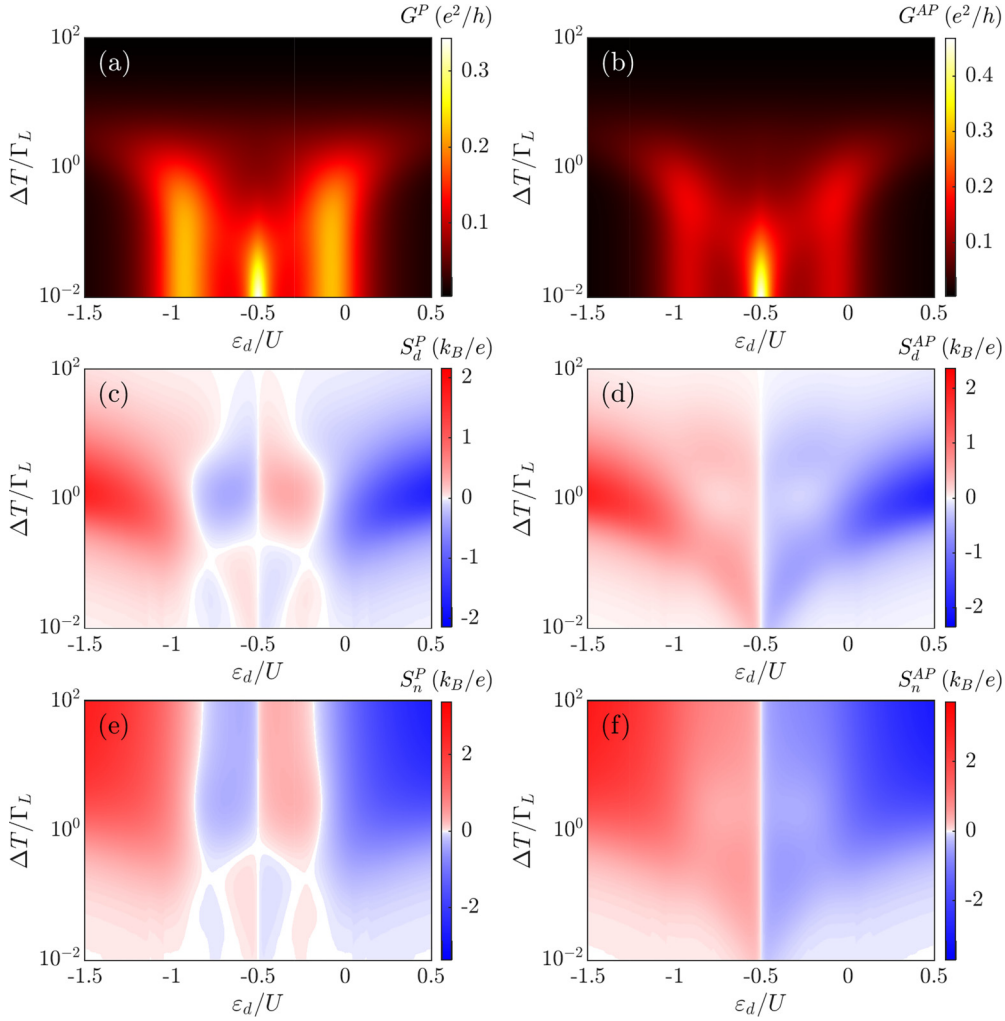

FIG. 6. (a), (b) The differential conductance G, (c), (d) the differential Seebeck coefficient S_d and (e), (f) the nonequilibrium Seebeck coefficient S_n in (first column) the parallel (P) and (second column) antiparallel (AP) configuration calculated as a function of ΔT and ε_d assuming linear response in voltage. The spin polarizations of both leads are equal to $p = 0.4$ and the other parameters are the same as in Fig. 3.

from the particle-hole symmetry point. The first sign change occurs when detuning is large enough to induce the exchange field that suppresses the Kondo effect. Further sign change occurs at the onset of conductance increase (as function of ε_d) due to the Hubbard resonance. This behavior extends to higher ΔT as long as the thermal gradient is smaller than the Kondo energy scale (or $\Delta\varepsilon_{\text{exch}}$). Otherwise, another sign change occurs as a function of ΔT, see Fig. 6(c). Very similar dependence can be observed in Fig. 6(e), which shows the nonequilibrium Seebeck coefficient S_n^P. The main difference can be seen for large ΔT, where S_n^P takes considerable values while S_d^P decreases, as explained earlier.

The situation is completely different in the case of the antiparallel configuration, where one does not see any additional sign changes, neither in S_d^{AP} nor in S_n^{AP}, other than the ones present across $\varepsilon_d = -U/2$, see Figs. 6(d) and 6(f). This can be understood by realizing that the interplay of exchange field with spin-dependent tunneling to the right contact hinders the splitting of the Kondo resonance as a function of the bias voltage. Consequently, one only observes a single resonance displaced from $V = 0$, cf. Fig. 3(c), which results in much more regular dependence of the differential and nonequilibrium Seebeck coefficients.

2. *The case of nonlinear potential bias and temperature gradient*

The nonequilibrium thermoelectric properties of the quantum dot coupled to both ferromagnetic leads are shown in Fig. 7. The first row corresponds to the case of parallel configuration of the leads' magnetizations. The differential conductance depicted in Fig. 7(a) exhibits the split Kondo anomaly, with side peaks of similar magnitude located at roughly the same distance from the zero bias. Both peaks die off with the temperature gradient around $\Delta T \approx 0.05\Gamma_L$, i.e. when thermal gradient exceeds the Kondo temperature.

At low ΔT the differential and nonequilibrium Seebeck coefficients exhibit similar bias voltage dependence to the case presented in Figs. 5(e) and 5(f), see Figs. 7(b) and 7(c). Now, however, the region of negative Seebeck coefficient is smaller. This can be attributed to the fact that the split Kondo resonance is more symmetric across the bias reversal in the case of parallel magnetic configuration, cf. Fig. 3(b). Unlike

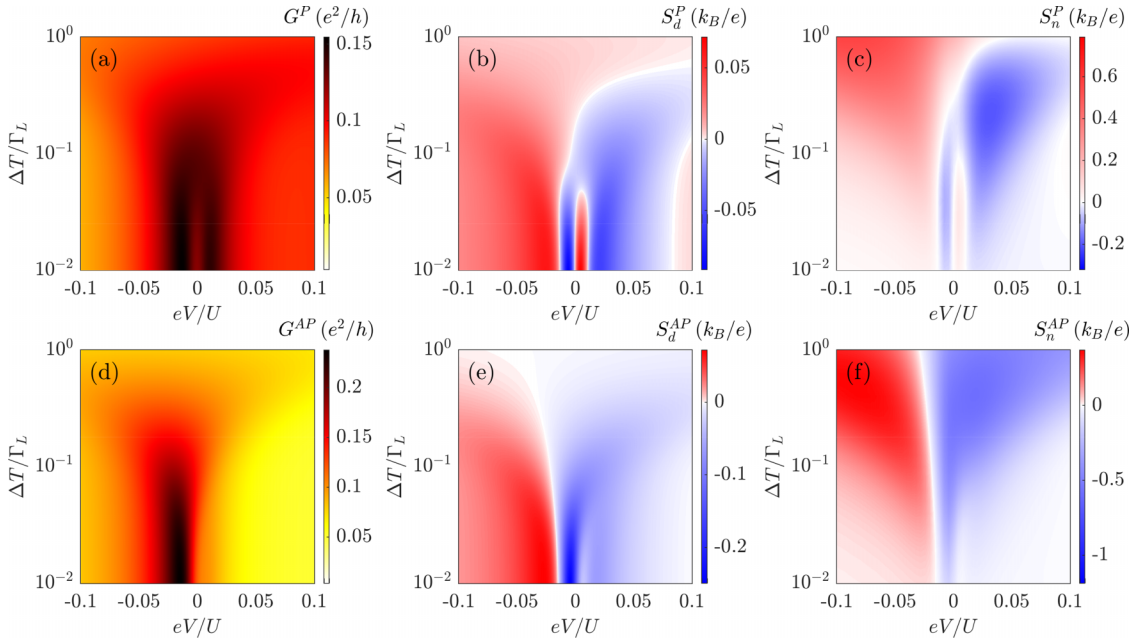

FIG. 7. (a), (d) The differential conductance G, (b), (e) the differential Seebeck coefficient S_d and (c), (f) the nonequilibrium Seebeck coefficient S_n as a function of the bias voltage and temperature gradient in the case of $\varepsilon_d = -U/3$. The first (second) row corresponds to the parallel (antiparallel) magnetic configuration of the system. The other parameters are the same as in Fig. 6.

in the case of nonmagnetic right lead, the sign changes at finite bias corresponding to the split Kondo peak persist as long as $\Delta T \lesssim T_K$ and disappear around comparable temperature gradient.

The case of antiparallel magnetic configuration of the system is presented in the second row of Fig. 7. Consistent with the discussion of Fig. 3(c), the differential conductance exhibits two conductance peaks but with a large difference in their magnitudes. The peak in the negative bias regime is far more pronounced than the miniscule peak one can observe in the positive regime. Just as in the case of other configurations, the peaks die out with increasing the temperature gradient but the negative bias peak survives till larger temperature gradients $\Delta T \approx 0.2\Gamma_L$, whereas the positive bias peak vanishes at temperature gradients as low as $\Delta T \approx 0.02\Gamma_L$.

The Seebeck coefficients S_d^{AP} and S_n^{AP}, shown in Figs. 7(e) and 7(f), respectively, demonstrate a similar behavior to the other configurations only at very low temperature gradients. However, now, instead of sign changes, one only observes suppression of the Seebeck coefficients at the corresponding values of the bias voltage associated with the exchange field. These suppressions extend to temperature gradients of the order of $\Delta T \approx 0.03\Gamma_L$, see Figs. 7(e) and 7(f).

C. Finite spin accumulation and the associated nonequilibrium spin Seebeck effect

In this section we consider the case when ferromagnetic contacts are characterized by slow spin relaxation, which can result in a finite spin accumulation [64,65]. Such a spin accumulation will induce a spin bias across the quantum dot. Here, we assume that the spin accumulation and the resulting spin-dependent chemical potential occurs only in the right lead. Thus, we define the induced spin bias as, $eV_s/2 = \mu_{R\uparrow} = -\mu_{R\downarrow}$ (keeping $\mu_L = 0$). The nonequilibrium spin bias across the quantum dot enables the spin chemical potentials to be tuned separately and thus the thermal bias induced transport can be different in the separate spin channels. The system can then exhibit interesting spin caloritronic properties, such as the spin Seebeck effect. The spin Seebeck coefficient S_s quantifies the magnitude and the direction of the spin current induced in the presence of a thermal bias [20]. Analogous to the differential Seebeck effect S_d, the differential spin Seebeck coefficient S_s in the nonlinear response regime can be defined as

$$S_s = -\left(\frac{dV_s}{d\Delta T}\right)_{I_s} = -\left(\frac{\partial I_s}{\partial \Delta T}\right)_{V_s} \Big/ \left(\frac{\partial I_s}{\partial V_s}\right)_{\Delta T}, \tag{10}$$

where $I_s = I_\uparrow(\mu_{R\uparrow}, \Delta T) - I_\downarrow(\mu_{R\downarrow}, \Delta T)$ is the net spin current flowing through the system. This quantity acts as a response over the spin current as a function of both the spin bias V_s and the temperature gradient ΔT. In addition to the net spin current, there can also exist a charge current $I = \sum_\sigma I_\sigma(\mu_{R\sigma}, \Delta T)$ flowing across the system originating solely from the thermal and the spin biases. We define the Seebeck coefficient that estimates the charge current in the presence of the spin bias as the charge Seebeck coefficient S [64]. The charge Seebeck coefficient S can thus be defined based on the response of charge current I as

$$S = -\left(\frac{dV_s}{d\Delta T}\right)_{I} = -\left(\frac{\partial I}{\partial \Delta T}\right)_{V_s} \Big/ \left(\frac{\partial I}{\partial V_s}\right)_{\Delta T}. \tag{11}$$

We first discuss the case of linear response in the spin bias V_s with large and finite temperature gradient ΔT, focusing on the differential spin Seebeck coefficient S_s and the charge Seebeck coefficient S. It is pertinent to note that the

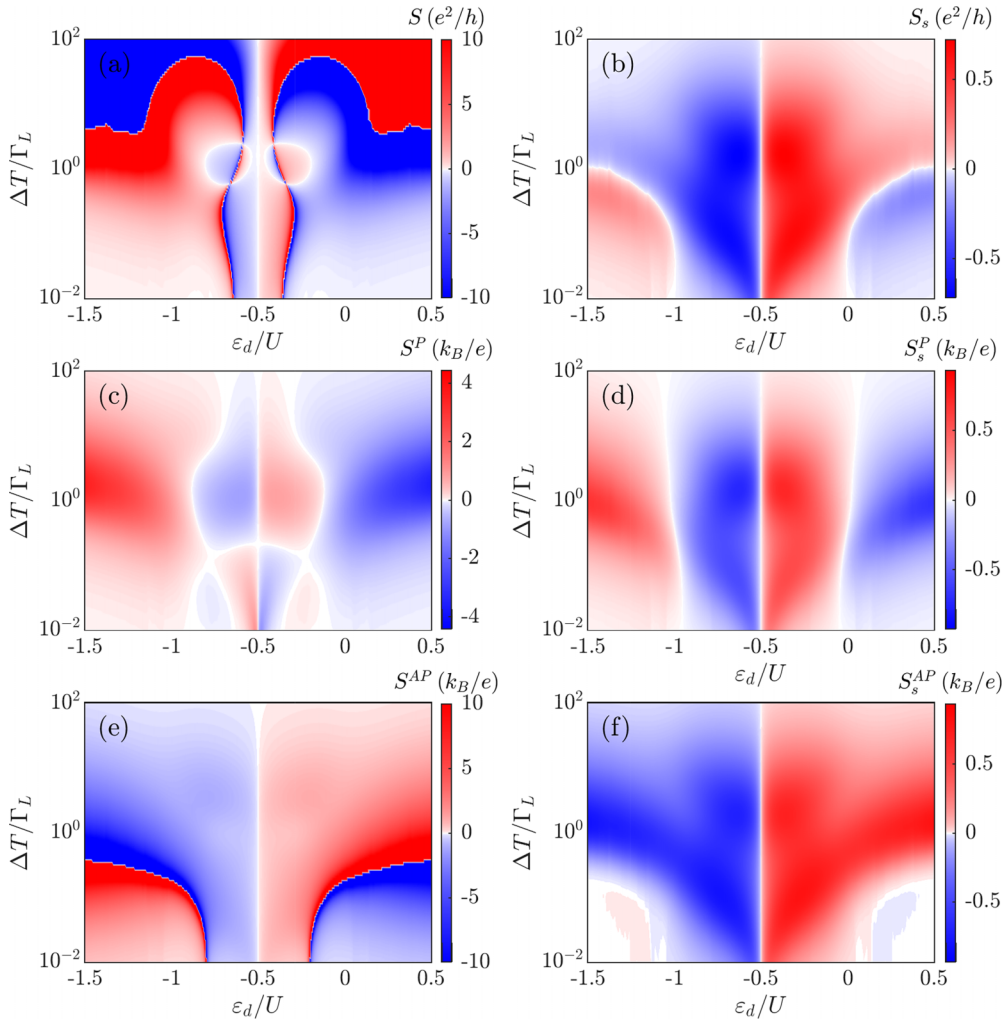

FIG. 8. The charge Seebeck (first column) and the spin Seebeck (second column) coefficients under nonlinear temperature gradient ΔT and linear response spin bias V_s as a function of the orbital level energy ε_d and ΔT. The first row corresponds to the case of nonmagnetic right lead, while the second (third) row presents the case of ferromagnetic right lead in the parallel (antiparallel) magnetic configuration of the system. The other parameters are the same as in Fig. 6.

nonequilibrium equivalent of the spin Seebeck coefficient $S_{s,n}$ tends to remain undefined in our considerations, since the magnitude of the spin bias fails to compensate for the thermally induced spin current in (*parts of*) the regimes considered. Hence in this paper, we limit our discussions to the differential spin Seebeck coefficient $S_s \equiv S_{s,d}$ in the case of different configurations. We further investigate the dependence of S_s and S on large and finite spin bias under applied temperature gradient.

1. The case of zero spin bias with nonlinear temperature gradient

Figure 8 shows the behavior of the charge Seebeck coefficients S, S^P, S^{AP} and the spin Seebeck coefficients S_s, S_s^P, S_s^{AP} for the case of nonmagnetic right lead, as well as the case of ferromagnetic lead in the parallel and antiparallel magnetic configurations, respectively. The first row of Fig. 8 shows the case of right lead with spin polarization $p = 0$, but with finite spin accumulation occurring from the spin-resolved transport through the quantum dot. Figure 8(a) displays the charge Seebeck S coefficient, which behaves similarly to the differential Seebeck effect S_d presented in Fig. 4 except some points of divergences. At temperature gradients smaller than Γ_L, there exist two additional sign changes, both in the local moment regime symmetric across the particle-hole symmetry point. The points of sign change spread out of the local moment regime for thermal biases $\Delta T \gtrsim 3\Gamma_L$. The sign changes of the Seebeck effect are also accompanied by large divergences in the magnitude of S. The additional sign changes and divergences originate from the behavior of the denominator in the definition of S, cf. Eq. (11). The denominator in Eq. (11), which can be represented as, $G^{cs} = (\partial I/\partial V_s)_{\Delta T}$, is the differential mixed conductance [64] that estimates the charge current in the presence of a spin bias, which can be either negative or positive, resulting in its zero crossing points causing the divergence. From a physical perspective, tuning the temperature gradient in these specific regimes will result in extraordinary changes in the induced charge current. Note that the colormaps in Figs. 8(a) and 8(e) have been truncated for readability.

The charge Seebeck coefficient for the parallel configuration [see Fig. 8(c)] nicely recreates the behavior seen in

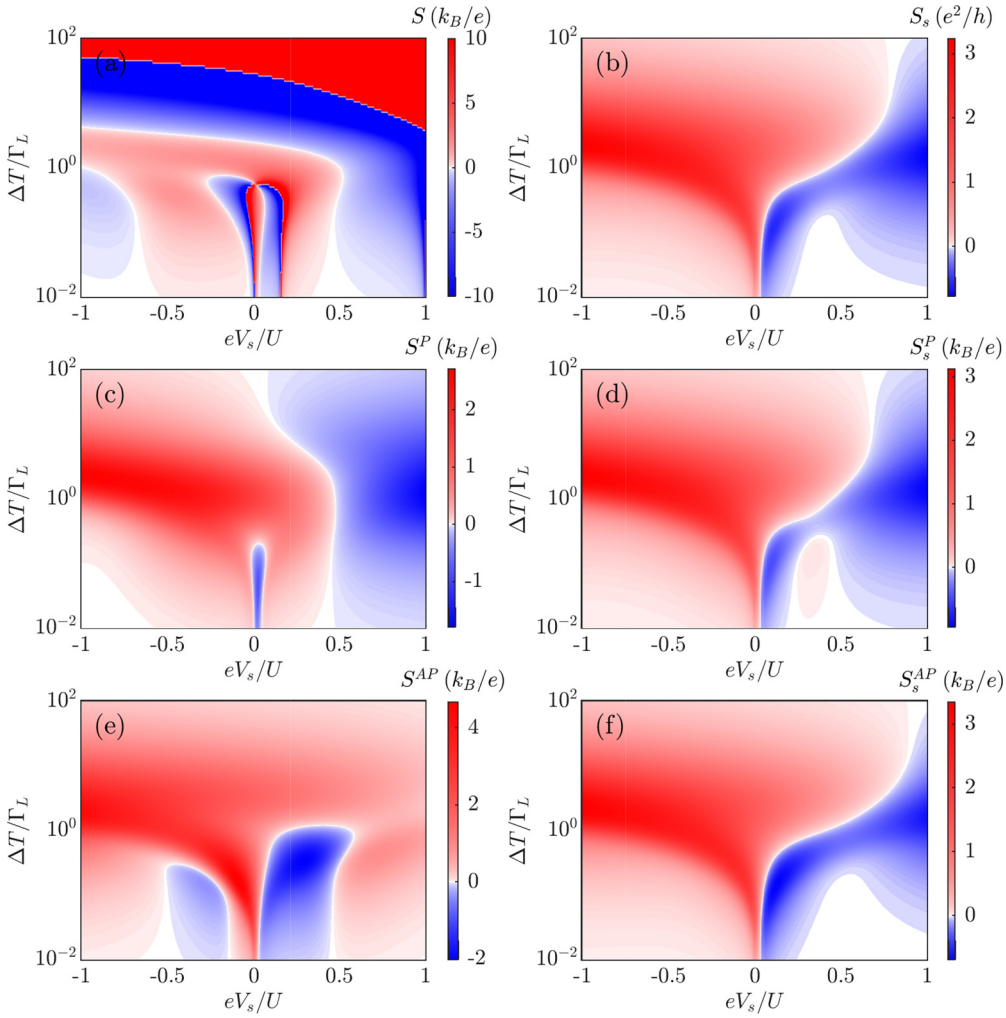

FIG. 9. The charge Seebeck (first column) and the spin Seebeck (second column) coefficients for the orbital level $\varepsilon_d = -U/3$ as a function of the applied spin bias V_s and ΔT. The first row corresponds to the case of nonmagnetic right lead, while the second (third) row presents the case of ferromagnetic right lead in the parallel (antiparallel) magnetic configuration of the system. The other parameters are the same as in Fig. 6.

Fig. 6(c). In the case of the parallel configuration, the relative scaling of the couplings in each spin channel on the right and left is the same, resulting in a non-negative G^{cs} and, thus, no divergences. Similarly, the charge Seebeck effect in the antiparallel configuration shown in Fig. 8(e) presents the behavior resembling the Seebeck coefficient discussed in Fig. 6(d), but overlaid by the divergences associated with G^{cs}. In this case, the additional sign changes start from inside the local moment regime at very low temperature gradients and move out of the local moment regime monotonously around $\Delta T \approx 10^{-1}\Gamma_L$.

The differential spin Seebeck coefficient S_s shown in Figs. 8(b), 8(d), and 8(f) for different lead configurations behave antisymmetrically across the particle-hole symmetry point ($\varepsilon_d = -U/2$). As can be seen, there exists a pronounced spin Seebeck coefficient in the local moment regime for all the configurations that dies off at $\Delta T \gtrsim 10\Gamma_L$. Such regions of considerable spin Seebeck effect have been observed in the linear response studies of symmetrically coupled quantum dots as a function of the global temperature T [27,33]. In addition to the sign change at the particle-hole symmetry point, at very low ΔT, S_s changes sign when moving out of the local moment regime (i.e., at $\varepsilon_d \approx -U, 0$). In the case of the nonmagnetic right lead, the region of sign change outside the local moment regime extends up to $\Delta T \approx \Gamma_L$, whereas for the antiparallel configuration the sign change extends only up to $\Delta T \approx 0.2\Gamma_L$. On the other hand, the sign change of the spin Seebeck coefficient in the local moment regime survives at thermal gradients even greater than $\Delta T \approx 10^2\Gamma_L$ for the parallel configuration.

2. *The case of nonlinear spin bias and temperature gradient*

The dependence of the nonlinear charge and spin Seebeck effects is shown in Fig. 9 for the case of orbital energy level $\varepsilon_d = -U/3$. The first column in Fig. 9 focuses on the charge Seebeck effect for various magnetic configurations of the system. For the case of nonmagnetic right lead, the charge Seebeck coefficient S changes sign multiple times as a function of eV_s at temperature gradients below $\Delta T \approx 0.5\Gamma_L$, see Fig. 9(a). Two among these sign changes (around $eV_s \approx 0.001\,U$ and $eV_s \approx 0.15\,U$) correspond to the zeros in the

mixed conductance G^{cs}, which can be identified from the divergence in S around the sign changes. The other two sign changes (around $eV_s \approx -0.05\,U$ and $eV_s \approx 0.03\,U$) originate from the zeros of the thermal response $-(\partial I/\partial \Delta T)_{V_s}$, i.e., the numerator in the definition of the charge Seebeck coefficient, cf. Eq. (10). As the temperature gradient increases, the regions of sign change introduced by G^{cs} and the thermal response become larger in the spin bias regime until around $\Delta T \approx \Gamma_L/3$ for the sign change associated with the mixed conductance, and until $\Delta T \approx \Gamma_L/2$ for the sign change associated with the thermal response. With further increase in the temperature gradient, the regions of sign change disappear. This happens around $\Delta T \gtrsim \Gamma_L/2$ for the sign change caused by the mixed conductance, and for $\Delta T \gtrsim 0.8\Gamma_L$ in the case of the sign change due to the thermal response. The remaining two sign changes at $eV_s \approx -U/2$ and $eV_s \approx U/2$ can be associated with the Hubbard resonances. The region of these sign changes disappears above temperature gradient $\Delta T \gtrsim 4\Gamma_L$. On the other hand, at $eV_s \approx 0$ and very large temperature gradients (around $\Delta T \gtrsim 10\Gamma_L$), there exists another sign change that originates from the zeros of G^{cs}. For positive eV_s, this sign change moves to lower ΔT, while for negative eV_s, the sign change moves to higher ΔT, see Fig. 9(a).

Figure 9(c) shows the charge Seebeck coefficient S^P corresponding to the system in the parallel magnetic configuration of ferromagnetic leads. We observe that there are two sign changes as a function of the spin bias eV_s. At low temperatures, $\Delta T \lesssim 0.01\Gamma_L$, the region of sign change appears between $eV_s \approx 0.005\,U$ and $eV_s \approx 0.5\,U$. One can identify that these sign changes originate solely from the thermal response of the current under spin bias. As can be seen in Fig. 9(c), the position of the sign changes in eV_s hardly depends on temperature gradient as long as it is lower than $\Delta T \approx 0.5\Gamma_L$. On the other hand, once $\Delta T \gtrsim 0.5\Gamma_L$, the negative region of S^P around $eV_s \approx 0.005\,U$ disappears. However, unlike in the previous case of S, the sign change around $eV_s \approx U/2$, which is due to the contribution from the Hubbard resonance, survives for large temperature gradients ΔT. This sign change moves closer to $V_s \approx 0$ when the temperature gradient ΔT is increased $\Delta T \gtrsim \Gamma_L$, see Fig. 9(c).

The charge Seebeck coefficient for the antiparallel configuration S^{AP} does not exhibit any sign change in the local moment regime apart from the particle-hole symmetry point $\varepsilon_d = -U/2$, as shown in Fig. 8(e). However, as a function of the spin bias eV_s, two new regions of sign change form in the dependence of S^{AP}. More specifically, one sign change occurs in the negative spin bias regime around $eV_s \approx -0.15\,U$, and the other one in the positive regime for $eV_s \approx 0.03\,U$. As can be seen in the figure, the negative values of the charge Seebeck effect extend until $|eV_s| \gtrsim U/2$. Furthermore, with increasing ΔT, the corresponding sign changes move further apart into the negative and positive spin bias regimes, respectively. On the other hand, for $\Delta T \gtrsim \Gamma_L$, S^{AP} becomes positive for all values of eV_s considered, see Fig. 8(e).

It is important to emphasize that the sign changes observed in the charge Seebeck coefficient as a function of spin bias eV_s do not correspond to the sign changes seen in the Seebeck coefficient as a function of eV, as discussed and presented in Figs. 5 and 7. This is associated with the fact that the generated current as a function of voltage V scans through each of the split Kondo resonances shown in Fig. 2 separately, resulting in the split peaks seen in the differential conductance and the corresponding sign changes in the Seebeck coefficients. However, as a function of the spin bias eV_s, the signatures from the split Kondo resonance cannot be identified directly in the generated current I. This is because for finite spin bias, $\mu_{R\uparrow} - \mu_{R\downarrow} = eV_s$, both split Kondo peaks contribute simultaneously, and the total current I is rescaled by relative couplings of the separate spin channels $\Gamma_{R\sigma}$. Hence, the sign changes in the charge Seebeck coefficient are solely resulting from the sign changes in the thermal response and the mixed charge conductance.

The spin Seebeck coefficient in the nonlinear spin bias regime is presented in the second column of Fig. 9. Figures 9(b), 9(d), and 9(f) show the case of the nonmagnetic right lead as well as ferromagnetic right lead in the parallel and antiparallel magnetic configuration of the nanojunction, respectively. As can be seen, the behavior of the spin Seebeck coefficient is qualitatively comparable for almost all configurations. From the discussion of the linear V_s case shown in Fig. 8, we observe that the differential spin Seebeck coefficient for $eV_s \approx 0$ does not change sign as a function of thermal gradient for all three configurations. Thus, for negative eV_s, S_s is positive irrespective of magnetic arrangement, see the right column of Fig. 9. On the other hand, for positive spin bias eV_s, one observes a sign change around $eV_s \approx 0.02\,U$, which moves to higher eV_s with increasing ΔT above $\Delta T \approx \Gamma_L$. Moreover, with further increasing eV_s, there is a region of suppressed S_s around $eV_s \approx 0.2\,U$, which extends to $eV_s \approx U/2$. Interestingly, one can note that the spin Seebeck effect in this region changes sign in the case of parallel configuration, thus introducing another sign change as a function of spin bias, see Fig. 9(d). This region disappears once $\Delta T \gtrsim 0.2\Gamma_L$.

IV. CONCLUDING REMARKS

In this paper we have analyzed the nonequilibrium spin-resolved thermoelectric properties of a ferromagnetic nanojunction consisting of a quantum dot/molecule asymmetrically coupled to external ferromagnetic leads. The considerations have been carried out by performing perturbative expansion with respect to the weakly coupled electrode, while the properties of quantum dot strongly coupled to ferromagnetic lead were extracted by numerical renormalization group method. The emphasis has been put on the signatures of the interplay between spin-resolved tunneling and strong electron correlations in the nonequilibrium spin-dependent thermopower of the system. In particular, we have determined the bias voltage and temperature gradient dependence of the differential and nonequilibrium Seebeck coefficients in different magnetic configurations of the system. We have observed new signatures in the Seebeck effect corresponding to the Kondo resonance and the regions where the ferromagnetic contact induced exchange field suppresses the Kondo effect, both in the potential bias and the temperature gradient. More specifically, we have demonstrated that the Seebeck coefficient exhibits new sign changes as a function of bias voltage, which are associated with the split Kondo resonance. These sign changes, depending on the transport region, extend to the temperature gradients on the order of the Kondo

temperature or of the temperature associated with the energy scale of the exchange field. Furthermore, we have investigated the influence of the spin accumulation in the leads, that gives rise to finite spin bias, on the Seebeck and spin Seebeck coefficients. The nonlinear charge Seebeck coefficient and the spin Seebeck coefficient showed points of sign changes in the presence of finite spin and thermal bias, indicating an intricate interplay of Kondo correlations with spin-resolved tunneling processes at nonequilibrium settings.

We believe that our work sheds new light on the spin-resolved nonequilibrium thermopower of correlated nanoscale junctions and, thus, provides a better understanding of thermoelectrics under finite temperature and voltage gradients. We also hope that our findings will foster further theoretical and experimental investigations of spin thermoelectric properties in fully nonequilibrium conditions.

As an outlook, we would like to notice that it would be of importance to explore the nonequilibrium thermoelectric transport properties of nanoscale systems strongly coupled to both left and right leads. Accurate treatment of correlations in such setups would however require resorting to more sophisticated numerical techniques, such as recently developed hybrid method of NRG and time-dependent density matrix renormalization group [66,67]. While addressing such a problem goes beyond the scope of the present paper, it definitely provides an important objective for future research endeavor.

ACKNOWLEDGMENT

This work was supported by the Polish National Science Centre from funds awarded through the decision No. 2017/27/B/ST3/00621. We also acknowledge the computing time at the Poznań Supercomputing and Networking Center.

[1] I. Žutić, J. Fabian, and S. Das Sarma, Spintronics: Fundamentals and applications, Rev. Mod. Phys. **76**, 323 (2004).

[2] G. E. W. Bauer, E. Saitoh, and B. J. van Wees, Spin caloritronics, Nat. Mater. **11**, 391 (2012).

[3] D. D. Awschalom, L. C. Bassett, A. S. Dzurak, E. L. Hu, and J. R. Petta, Quantum spintronics: Engineering and manipulating atom-like spins in semiconductors, Science **339**, 1174 (2013).

[4] A. Hirohata, K. Yamada, Y. Nakatani, I.-L. Prejbeanu, B. Diény, P. Pirro, and B. Hillebrands, Review on spintronics: Principles and device applications, J. Magn. Magn. Mater. **509**, 166711 (2020).

[5] G. D. Mahan and J. O. Sofo, The best thermoelectric, Proc. Natl. Acad. Sci. USA **93**, 7436 (1996).

[6] A. Dhar, Heat transport in low-dimensional systems, Adv. Phys. **57**, 457 (2008).

[7] Y. Dubi and M. Di Ventra, Thermoelectric effects in nanoscale junctions, Nano Lett. **9**, 97 (2009).

[8] Y. Dubi and M. Di Ventra, *Colloquium*: Heat flow and thermoelectricity in atomic and molecular junctions, Rev. Mod. Phys. **83**, 131 (2011).

[9] G. Benenti, G. Casati, K. Saito, and R. S. Whitney, Fundamental aspects of steady-state conversion of heat to work at the nanoscale, Phys. Rep. **694**, 1 (2017).

[10] M. Josefsson, A. Svilans, A. M. Burke, E. A. Hoffmann, S. Fahlvik, C. Thelander, M. Leijnse, and H. Linke, A quantum-dot heat engine operating close to the thermodynamic efficiency limits, Nat. Nanotechnol. **13**, 920 (2018).

[11] J. Kondo, Resistance minimum in dilute magnetic alloys, Prog. Theor. Phys. **32**, 37 (1964).

[12] A. C. Hewson, *The Kondo Problem to Heavy Fermions*, Cambridge Studies in Magnetism (Cambridge University Press, Cambridge, 1993).

[13] D. Goldhaber-Gordon, H. Shtrikman, D. Mahalu, D. Abusch-Magder, U. Meirav, and M. A. Kastner, Kondo effect in a single-electron transistor, Nature (London) **391**, 156 (1998).

[14] S. M. Cronenwett, T. H. Oosterkamp, and L. P. Kouwenhoven, A tunable Kondo effect in quantum dots, Science **281**, 540 (1998).

[15] T. A. Costi and V. Zlatić, Thermoelectric transport through strongly correlated quantum dots, Phys. Rev. B **81**, 235127 (2010).

[16] A. Svilans, M. Josefsson, A. M. Burke, S. Fahlvik, C. Thelander, H. Linke, and M. Leijnse, Thermoelectric characterization of the Kondo resonance in nanowire quantum dots, Phys. Rev. Lett. **121**, 206801 (2018).

[17] B. Dutta, D. Majidi, A. García Corral, P. A. Erdman, S. Florens, T. A. Costi, H. Courtois, and C. B. Winkelmann, Direct probe of the Seebeck coefficient in a Kondo-correlated single-quantum-dot transistor, Nano Lett. **19**, 506 (2019).

[18] C. Hsu, T. A. Costi, D. Vogel, C. Wegeberg, M. Mayor, H. S. J. van der Zant, and P. Gehring, Magnetic-field universality of the Kondo effect revealed by thermocurrent spectroscopy, Phys. Rev. Lett. **128**, 147701 (2022).

[19] J. Barnaś and I. Weymann, Spin effects in single-electron tunnelling, J. Phys.: Condens. Matter **20**, 423202 (2008).

[20] K. Uchida, S. Takahashi, K. Harii, J. Ieda, W. Koshibae, K. Ando, S. Maekawa, and E. Saitoh, Observation of the spin Seebeck effect, Nature (London) **455**, 778 (2008).

[21] H. Adachi, K.-I. Uchida, E. Saitoh, and S. Maekawa, Theory of the spin Seebeck effect, Rep. Prog. Phys. **76**, 036501 (2013).

[22] J. Martinek, M. Sindel, L. Borda, J. Barnaś, J. König, G. Schön, and J. von Delft, Kondo effect in the presence of itinerant-electron ferromagnetism studied with the numerical renormalization group method, Phys. Rev. Lett. **91**, 247202 (2003).

[23] A. N. Pasupathy, R. C. Bialczak, J. Martinek, J. E. Grose, L. A. K. Donev, P. L. McEuen, and D. C. Ralph, The Kondo effect in the presence of ferromagnetism, Science **306**, 86 (2004).

[24] K. Hamaya, M. Kitabatake, K. Shibata, M. Jung, M. Kawamura, K. Hirakawa, T. Machida, T. Taniyama, S. Ishida, and Y. Arakawa, Kondo effect in a semiconductor quantum dot coupled to ferromagnetic electrodes, Appl. Phys. Lett. **91**, 232105 (2007).

[25] I. Weymann, Finite-temperature spintronic transport through Kondo quantum dots: Numerical renormalization group study, Phys. Rev. B **83**, 113306 (2011).

[26] M. Krawiec and K. I. Wysokiński, Thermoelectric effects in strongly interacting quantum dot coupled to ferromagnetic leads, Phys. Rev. B **73**, 075307 (2006).

[27] I. Weymann and J. Barnaś, Spin thermoelectric effects in Kondo quantum dots coupled to ferromagnetic leads, Phys. Rev. B **88**, 085313 (2013).

[28] Ł. Karwacki, P. Trocha, and J. Barnaś, Spin-dependent thermoelectric properties of a Kondo-correlated quantum dot with Rashba spin-orbit coupling, J. Phys.: Condens. Matter **25**, 505305 (2013).

[29] K. P. Wójcik and I. Weymann, Thermopower of strongly correlated T-shaped double quantum dots, Phys. Rev. B **93**, 085428 (2016).

[30] Ł. Karwacki and P. Trocha, Spin-dependent thermoelectric effects in a strongly correlated double quantum dot, Phys. Rev. B **94**, 085418 (2016).

[31] K. P. Wójcik and I. Weymann, Strong spin Seebeck effect in Kondo T-shaped double quantum dots, J. Phys.: Condens. Matter **29**, 055303 (2017).

[32] G. Górski and K. Kucab, Effect of assisted hopping on spin-dependent thermoelectric transport through correlated quantum dot, Phys. B **545**, 337 (2018).

[33] A. Manaparambil and I. Weymann, Spin Seebeck effect of correlated magnetic molecules, Sci. Rep. **11**, 9192 (2021).

[34] P. Majek, K. P. Wójcik, and I. Weymann, Spin-resolved thermal signatures of Majorana-Kondo interplay in double quantum dots, Phys. Rev. B **105**, 075418 (2022).

[35] M. A. Sierra and D. Sánchez, Strongly nonlinear thermovoltage and heat dissipation in interacting quantum dots, Phys. Rev. B **90**, 115313 (2014).

[36] A. Svilans, M. Leijnse, and H. Linke, Experiments on the thermoelectric properties of quantum dots, C. R. Phys. **17**, 1096 (2016).

[37] M. A. Sierra, R. López, and D. Sánchez, Fate of the spin-$\frac{1}{2}$ Kondo effect in the presence of temperature gradients, Phys. Rev. B **96**, 085416 (2017).

[38] A. Khedri, T. A. Costi, and V. Meden, Nonequilibrium thermoelectric transport through vibrating molecular quantum dots, Phys. Rev. B **98**, 195138 (2018).

[39] U. Eckern and K. I. Wysokiński, Two- and three-terminal far-from-equilibrium thermoelectric nano-devices in the Kondo regime, New J. Phys. **22**, 013045 (2020).

[40] A. Manaparambil and I. Weymann, Nonequilibrium Seebeck effect and thermoelectric efficiency of Kondo-correlated molecular junctions, Phys. Rev. B **107**, 085404 (2023).

[41] J. Bauer, J. I. Pascual, and K. J. Franke, Microscopic resolution of the interplay of Kondo screening and superconducting pairing: Mn-phthalocyanine molecules adsorbed on superconducting Pb(111), Phys. Rev. B **87**, 075125 (2013).

[42] C. Xu, C.-L Chiang, Z. Han, and W. Ho, Nature of asymmetry in the vibrational line shape of single-molecule inelastic electron tunneling spectroscopy with the STM, Phys. Rev. Lett. **116**, 166101 (2016).

[43] M. Gruber, A. Weismann, and R. Berndt, The Kondo resonance line shape in scanning tunnelling spectroscopy: Instrumental aspects, J. Phys.: Condens. Matter **30**, 424001 (2018).

[44] N. Xin, J. Guan, C. Zhou, X. Chen, C. Gu, Y. Li, M. A. Ratner, A. Nitzan, J. F. Stoddart, and X. Guo, Concepts in the design and engineering of single-molecule electronic devices, Nat. Rev. Phys. **1**, 211 (2019).

[45] M. Žonda, O. Stetsovych, R. Korytár, M. Ternes, R. Temirov, A. Raccanelli, F. S. Tautz, P. Jelínek, T. Novotný, and M. Švec, Resolving ambiguity of the Kondo temperature determination in mechanically tunable single-molecule Kondo systems, J. Phys. Chem. Lett. **12**, 6320 (2021).

[46] Y. Xing, H. Chen, B. Hu, Y. Ye, W. A. Hofer, and H.-J. Gao, Reversible switching of Kondo resonance in a single-molecule junction, Nano Res. **15**, 1466 (2022).

[47] M. Krawiec and K. I. Wysokiński, Thermoelectric phenomena in a quantum dot asymmetrically coupled to external leads, Phys. Rev. B **75**, 155330 (2007).

[48] T. K. T. Nguyen, M. N. Kiselev, and V. E. Kravtsov, Thermoelectric transport through a quantum dot: Effects of asymmetry in Kondo channels, Phys. Rev. B **82**, 113306 (2010).

[49] D. Pérez Daroca, P. Roura-Bas, and A. A. Aligia, Enhancing the nonlinear thermoelectric response of a correlated quantum dot in the Kondo regime by asymmetrical coupling to the leads, Phys. Rev. B **97**, 165433 (2018).

[50] K. G. Wilson, The renormalization group: Critical phenomena and the Kondo problem, Rev. Mod. Phys. **47**, 773 (1975).

[51] R. Bulla, T. A. Costi, and T. Pruschke, Numerical renormalization group method for quantum impurity systems, Rev. Mod. Phys. **80**, 395 (2008).

[52] S. Csonka, I. Weymann, and G. Zarand, An electrically controlled quantum dot based spin current injector, Nanoscale **4**, 3635 (2012).

[53] P. Tulewicz, K. Wrześniewski, S. Csonka, and I. Weymann, Large voltage-tunable spin valve based on a double quantum dot, Phys. Rev. Appl. **16**, 014029 (2021).

[54] We used the open-access Budapest Flexible DM-NRG code, http://www.phy.bme.hu/~dmnrg/; O. Legeza, C. P. Moca, A. I. Tóth, I. Weymann, G. Zaránd, Manual for the flexible DM-NRG code, arXiv:0809.3143 (unpublished).

[55] A. Weichselbaum and J. von Delft, Sum-rule conserving spectral functions from the numerical renormalization group, Phys. Rev. Lett. **99**, 076402 (2007).

[56] A. Dorda, M. Ganahl, S. Andergassen, W. von der Linden, and E. Arrigoni, Thermoelectric response of a correlated impurity in the nonequilibrium Kondo regime, Phys. Rev. B **94**, 245125 (2016).

[57] M. Leijnse, M. R. Wegewijs, and K. Flensberg, Nonlinear thermoelectric properties of molecular junctions with vibrational coupling, Phys. Rev. B **82**, 045412 (2010).

[58] J. Azema, P. Lombardo, and A.-M. Daré, Conditions for requiring nonlinear thermoelectric transport theory in nanodevices, Phys. Rev. B **90**, 205437 (2014).

[59] P. A. Erdman, F. Mazza, R. Bosisio, G. Benenti, R. Fazio, and F. Taddei, Thermoelectric properties of an interacting quantum dot based heat engine, Phys. Rev. B **95**, 245432 (2017).

[60] J. Martinek, Y. Utsumi, H. Imamura, J. Barnaś, S. Maekawa, J. König, and G. Schön, Kondo effect in quantum dots coupled to ferromagnetic leads, Phys. Rev. Lett. **91**, 127203 (2003).

[61] J. R. Hauptmann, J. Paaske, and P. E. Lindelof, Electric-field-controlled spin reversal in a quantum dot with ferromagnetic contacts, Nat. Phys. **4**, 373 (2008).

[62] M. Gaass, A. K. Hüttel, K. Kang, I. Weymann, J. von Delft, and Ch. Strunk, Universality of the Kondo effect in quantum dots with ferromagnetic leads, Phys. Rev. Lett. **107**, 176808 (2011).

[63] F. D. M. Haldane, Scaling theory of the asymmetric Anderson model, Phys. Rev. Lett. **40**, 416 (1978).

[64] R. Świrkowicz, J. Barnaś, and M. Wilczyński, Transport through a quantum dot subject to spin and charge bias, J. Magn. Magn. Mater. **321**, 2414 (2009).

[65] R. Świrkowicz, M. Wierzbicki, and J. Barnaś, Thermoelectric effects in transport through quantum dots attached to ferromagnetic leads with noncollinear magnetic moments, Phys. Rev. B **80**, 195409 (2009).

[66] F. Schwarz, I. Weymann, J. von Delft, and A. Weichselbaum, Nonequilibrium steady-state transport in quantum impurity models: A thermofield and quantum quench approach using matrix product states, Phys. Rev. Lett. **121**, 137702 (2018).

[67] A. Manaparambil, A. Weichselbaum, J. von Delft, and I. Weymann, Nonequilibrium spintronic transport through Kondo impurities, Phys. Rev. B **106**, 125413 (2022).